Electronic Supplementary Information (ESI)

Bioinspired Interfacial Design to Toughen Carbon Nanotube Fibers

Shaojun Dong,[#,a,b,c] Zhongdong Gan,[#,d] Xinyan Chen,[a] Ying Pei,[e] Bin Li,[,a,b,c] Jing Ren,[*,a] Yanlei Wang,[*,f] Hongyan He,[f] and Shengjie Ling[*,a]*

[a]School of Physical Science and Technology, ShanghaiTech University, 393 Middle Huaxia Road, Shanghai, 201210, China

[b]Shanghai Institute of Applied Physics, Chinese Academy of Sciences, Shanghai 201800, China

[c]Shanghai Synchrotron Radiation Facility, Shanghai Advanced Research Institute, Chinese Academy of Sciences, Shanghai 201204, China

[d]School of Chemical Engineering & Technology, Tianjin University, Tianjin, 300072, China

[e]School of Materials Science and Engineering, Zhengzhou University, Zhengzhou, 450001, China.

[f]Beijing Key Laboratory of Ionic Liquids Clean Process, Institute of Process Engineering, Chinese Academy of Sciences, Beijing 100190, China

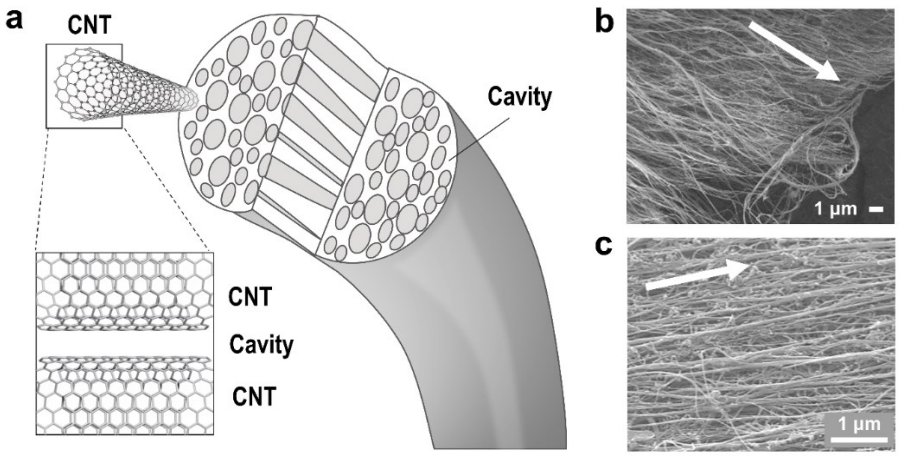

Fig. S1 Hierarchical interfaces in CNT. (a) Schematic illustration of the hierarchical interfaces in CNT fibers. (b) Cross-sectional SEM image of the CNT fibers. (c) Surface SEM image of CNT fibers.

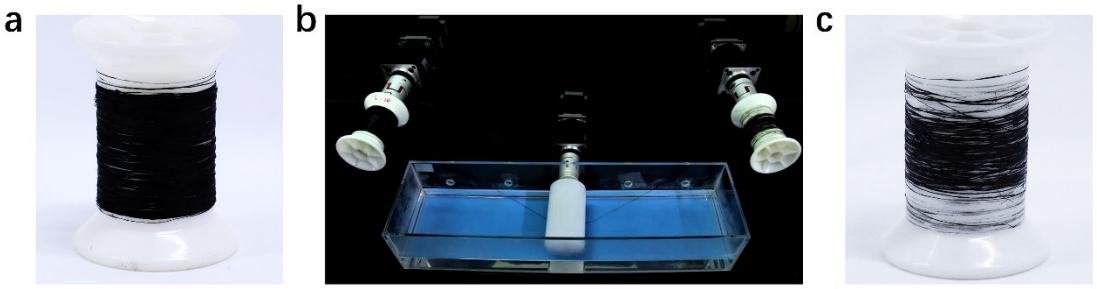

Fig. S2 Photographs of CNT and CNT-ISF fiber. (a) CNT fiber. (b) The continuous spinning of CNT-ISF fiber. (c) CNT-ISF fiber.

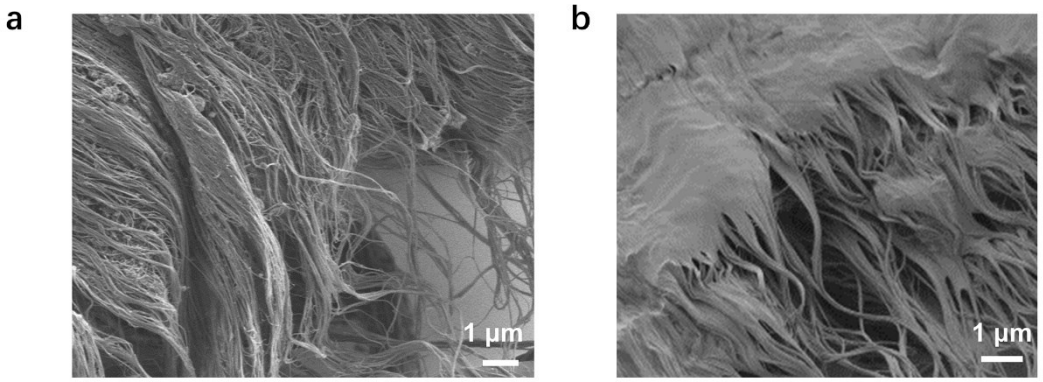

Fig. S3 SEM image of cross section of the CNT fiber (a) and CNT-ISF fiber (b) after being tensile to failure.

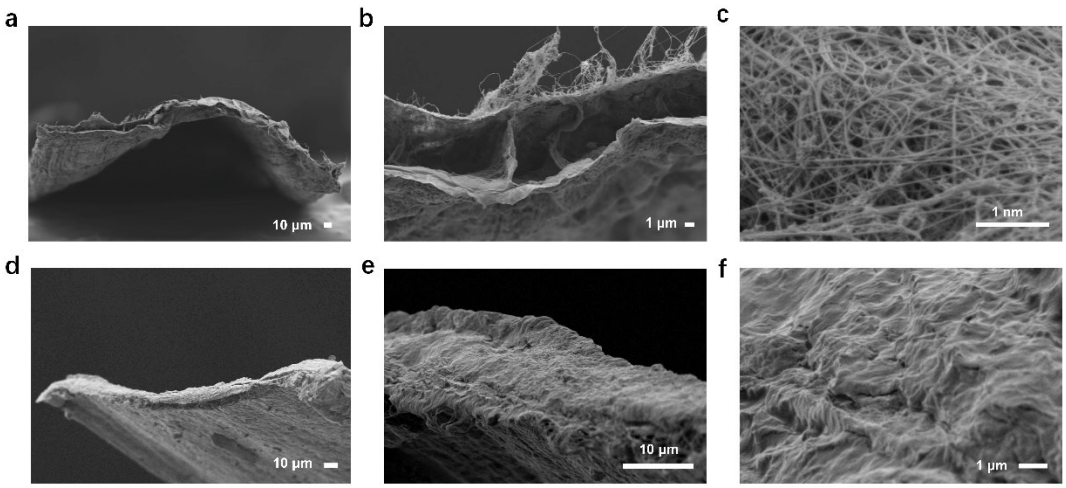

Fig. S4 SEM image of cross section of the CNT fiber (a, b, c) and CNT-ISF fiber (d, e, f).

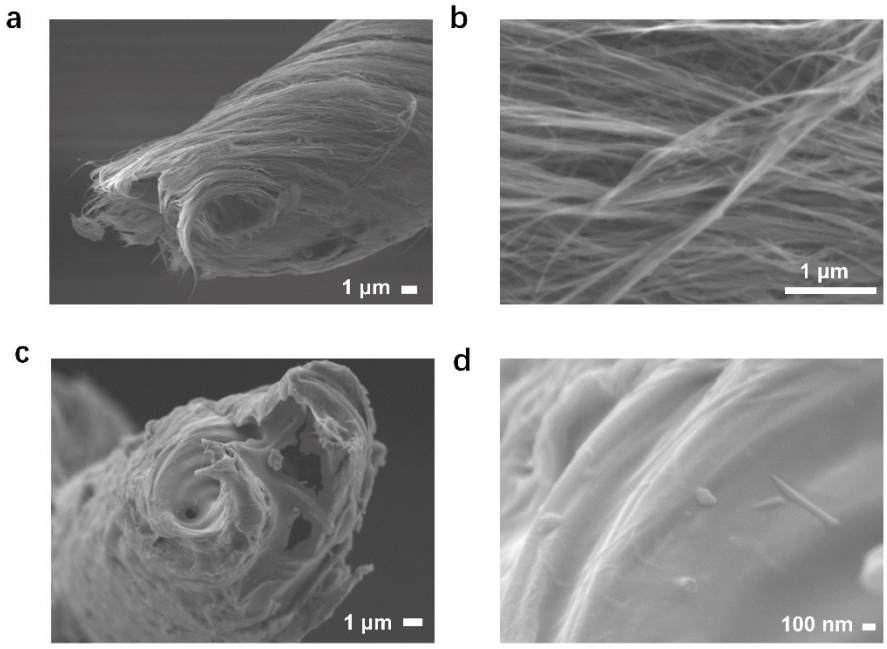

Fig. S5 SEM image of cross section of the stronger CNT fiber (a, b) and stronger CNT-ISF fiber (c, d).

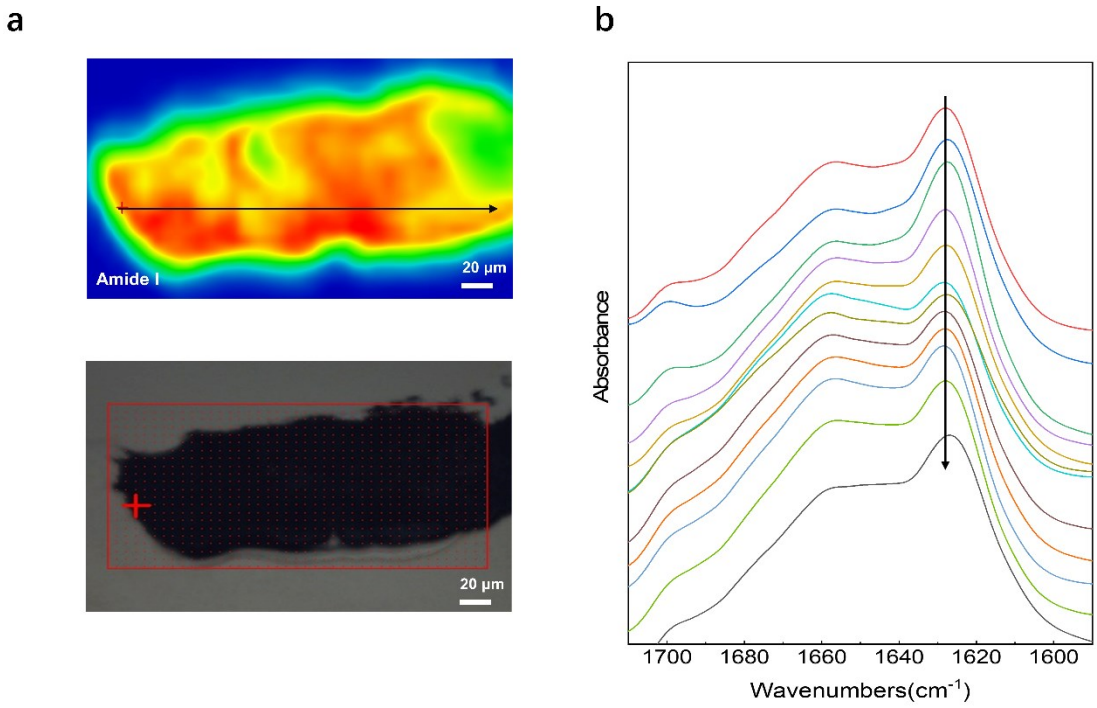

Fig. S6 S-FTIR spectroscopic images of CNT-ISF fiber. (a) S-FTIR spectroscopic images of CNT-ISF fiber slice by integrating the characteristic peak of the silk at 1628 cm^{-1} (amide I). (b) The single-pixel spectrums extracted along the direction indicated by the black arrow in (a).

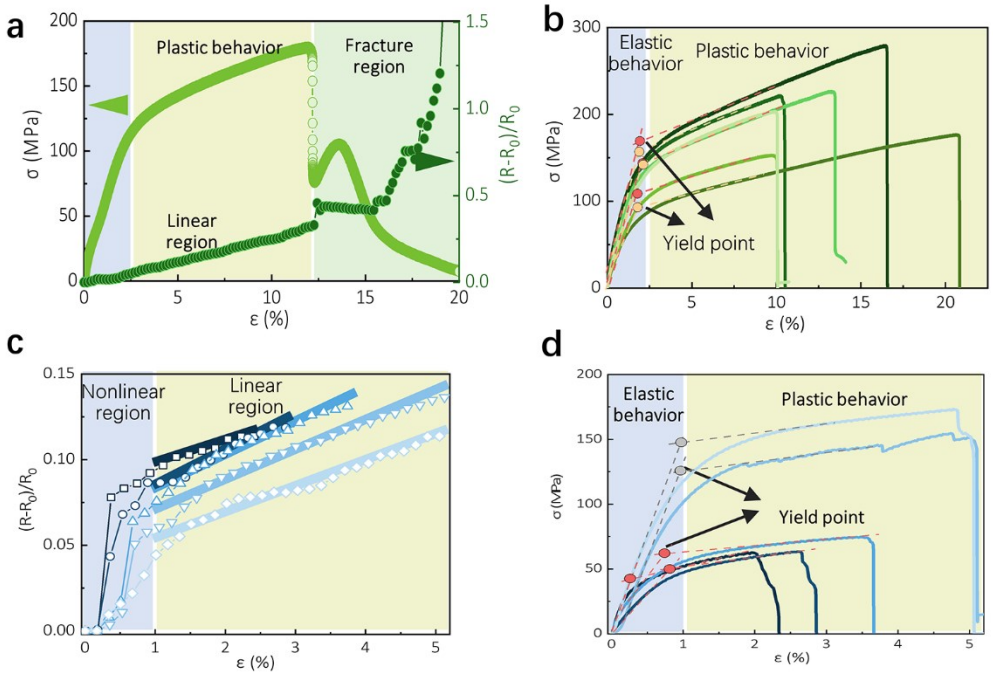

Fig. S7 Mechanical characteristics and electrical–mechanical response behavior of CNT and CNT-ISF fiber. (a) The left axis is the stress–strain relationship of CNT-ISF fiber, and the right axis is the relationship between the relative change rate of resistance and tensile strain of CNT-ISF fiber. (b) Stress–strain curves of the CNT-ISF fiber with a tensile speed of 2 mm min^{-1}. (c) The relationship between the relative change rate of resistance and tensile strain of CNT. (d) Stress–strain curves of the CNT with a tensile speed of 2 mm min^{-1}.

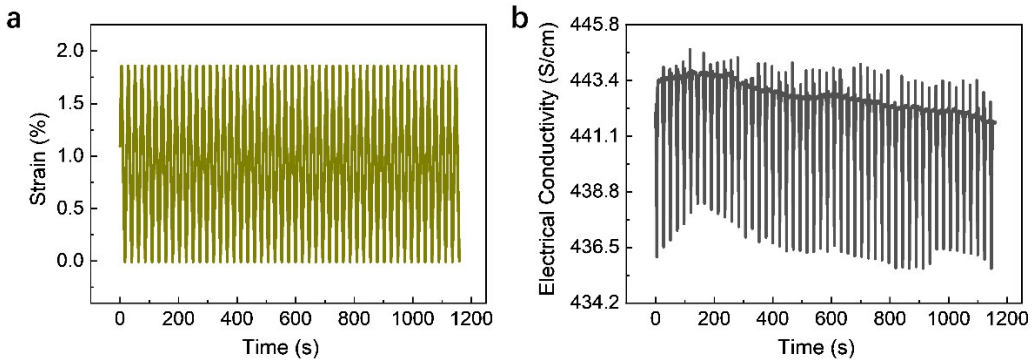

Fig. S8 Electrical conductivity changes of the CNT-ISF fibers during cyclic stretching-releasing with the maximum deformation of 1.8% in each cycle. (a) Strain–time curves of the CNT-ISF fiber in the cyclic stretching-releasing test. (b) Electrical conductivity–time curves of the CNT-ISF fiber in the cyclic stretching-releasing test.

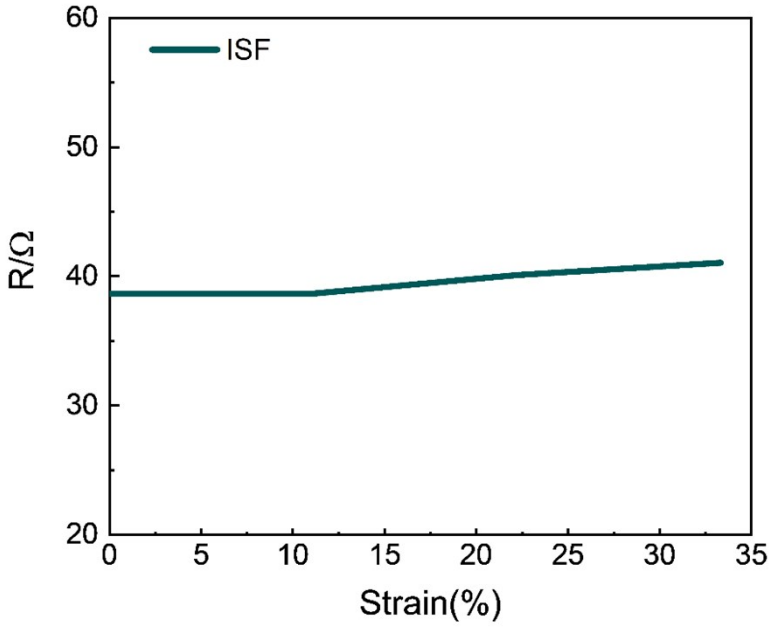

Fig. S9 The relationship between the resistance and tensile strain of ISF.

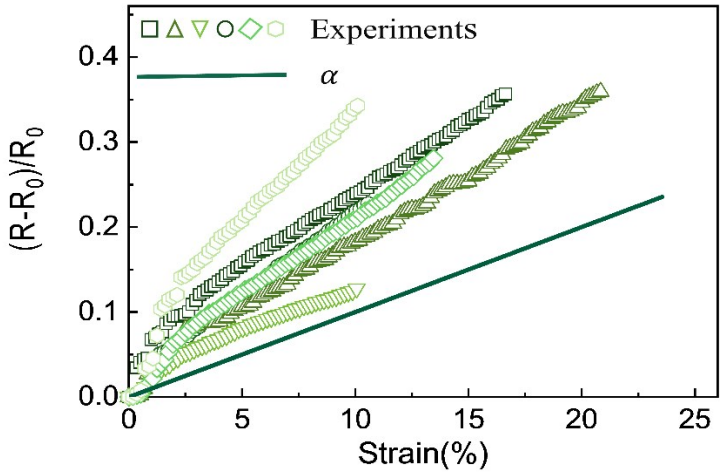

Fig. S10 The experimental and the geometric coefficient of resistance caused quantitative relationship between the relative change rate of resistance and tensile strain of CNT-ISF fiber.

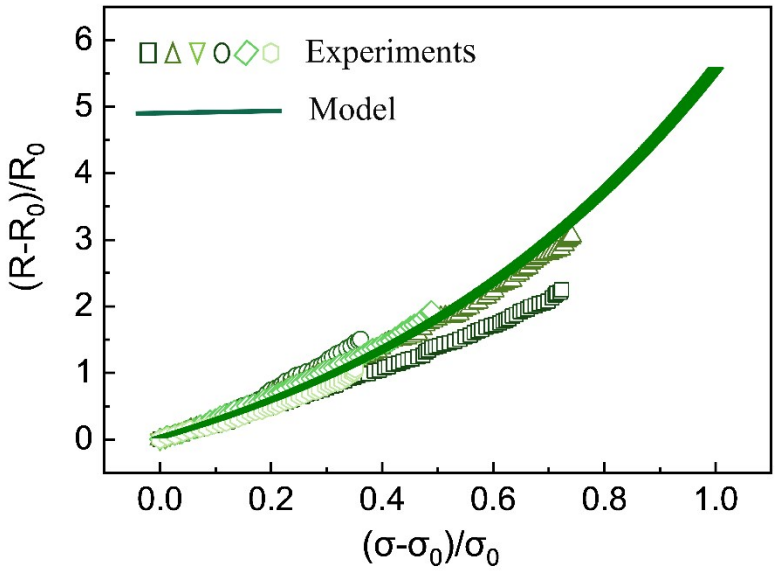

Fig. S11 The experimental and model-predicted quantitative relationship between relative change in resistance and tensile stress, Eq. (9).

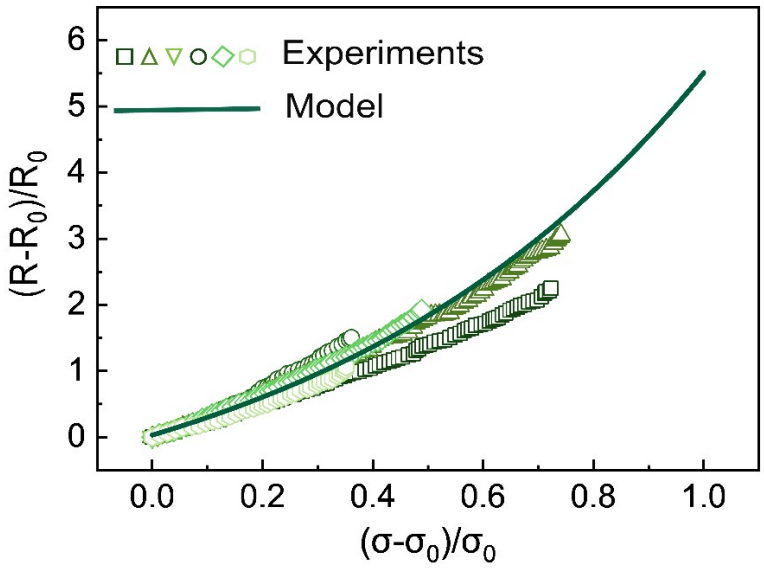

Fig. S12 The experimental and model-predicted quantitative relationship between relative change in resistance and tensile stress, Eq. (11).

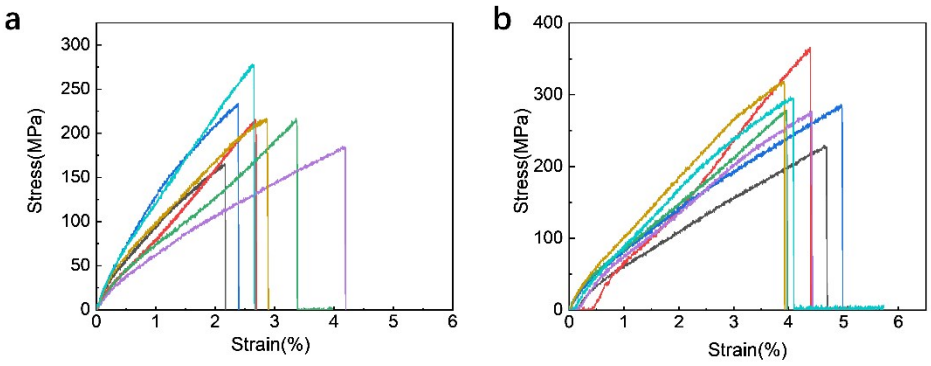

Fig. S13 Mechanical characteristics of raw CNT fibers produced by CVD and dry spinning method and the corresponding CNT-ISF fibers. (a) Stress–strain curves of the CNT with a tensile speed of 2 mm min^{-1}. (b) Stress–strain curves of the CNT-ISF fiber with a tensile speed of 2 mm min^{-1}.

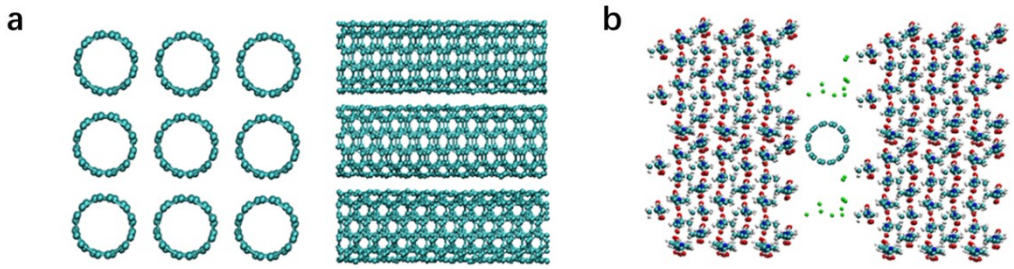

Fig. S14 Schematic configuration of (a) CNT and (b) CNT-ISF system.

Tab. S1 Comparison of diameter, mechanical properties, and conductivity of different natural and synthetic fibers reported in the literature.

Materials	Diameter (μm)	Strength (MPa)	Strain (%)	Modulus (GPa)	Toughness (MJ/m^3)	Conductivity (S/m)	Ref
CNT fiber	91.6	113.6	4.2	10.2	4.1	47234.02	This work
CNT-ISF fiber	75.4	209.2	13.6	8	21.6	44012.85	This work
Stronger CNT fiber	19.9	214	2.9	8.8	3.2	31137.80	This work
Stronger CNT-ISF fiber	18	290	4.3	7.6	6.7	21067.52	This work
B. *mori*[a)] silk	/	723	13.3	18.9	67.6	/	[1]
B. *mori* silk/MWCNTs[b)]	60-100	225	17	4.3	22	20	[2]
B. *mori* silk/CNT	20	420	59	11	186	/	[3]
N. clavipes[c)] spider silk	3	880-970	17-18	11-13	110	/	[4]
N. clavipes spider silk /MWCNTs	8	600	73	7	290	1200-1500	[5]
Polyurethane /PEDOT:PSS[d)]	80	52	440	0.01	66	70	[6]
PEDOT:PSS	10	86	12.5	2.4	8.3	800	[7]
PEDOT:PSS -SWNT[e)]	14	180	8	4	10.3	45000	[8]
PEDOT:PSS /CNT	10	215	13	4	23	2500	[9]
PPy[f)]-Alg-CNT	~93	~250	~10	10	1.8-16.5	200-1000	[10]
Silicone Elastomer/CNT	1856	0.4	600	0.067	1.2	0.1-1	[11]
SIBS[g)]/CNT	230	3	358	0.01	~5.37	4-9	[12]
SWCNT/ODCB[h)]	18	~1391.8	~4.3	~35.2	~31.9	65	[13]
Graphene fiber	~102	140	~5.8	7.7	4.4	~2500	[14]
SF[i)] nanofibril /graphene hybrids	47000	77-86	0.8-1.6	6-10	0.3-0.6	0.1-1.1	[15]
Graphene/SF	2000	49-242	2.2-8.1	4-6	0.7-11.6	0.032-67	[16]
Graphene/SF/Ca^{2+}	2000	0.5-5.9	202-611	0.004-0.135	3.3-13.9	0.032-0.21	[16]
Polyolefin Elastomer /Ag nanowires	300	10^{-6}	560	10^{-6}	4×10^{-6}	4000	[17]
High tensile steel	/	1500	0.8	200	6	1.45×10^{6}	[18,19]
PPy/rGO[j)]	61	85	7	4	4.2	1800	[20]
Carbon fiber	5-10	4000	1.3	300	25	55600-909000	[13,18]
Kevlar 49 fiber	12	3600	2.7	130	50	/	[18,21]

Abbreviations: [a)]*B. mori*, *Bombyx mori*; [b)]*N. Clavipes*, *Nephila clavipes*; [c)]MWCNTs, multiwall carbon nanotubes; [d)]PEDOT:PSS, poly(3,4-ethylenedioxythiophene)-poly(styrenesulfonate); [e)]SWNT, single walled carbon nanotubes; [f)]PPy, polypyrrole; [g)]SIBS, poly(styrene-β-isobutylene-β-styrene); [h)]ODCB,O-dichlorobenzene; [i)]SF, silk fibroin; [j)]rGO, reduced graphene oxide.

Tab. S2 The standard for classifying the diameter, mechanical properties, and conductivity performance of different natural and synthetic fibers.

Grade	Strain (%)	Strength (MPa)	Toughness (MJ/m^3)	Diameter (μm)	Conductivity (S/m)
1	<5	<10	<5	>100	<100
2	5-10	10-100	5-20	50-100	100-1000
3	10-100	100-200	20-50	10-50	1000-10000
4	100-500	200-500	50-200	5-10	10000-50000
5	>500	>500	>200	<5	>50000

Tab. S3 Lennard-Jones parameters and charges of SF and CNT.

Atom	μ (Å)	ϵ (kcal/mol)	Charge (e)
CNT			
C	**3.851**	**0.105**	**0.0**
Silk (OPLS)			
C1	3.6170	0.1480	0.37
O1	2.8598	0.2280	-0.15
C3	3.8754	0.0390	-0.30
H1	2.4500	0.0380	0.10
N3	3.5012	0.1670	-0.58
C2	3.8754	0.0390	0.12
H2	2.4400	0.0300	0.14
C4	3.8754	0.0390	0.02
C5	3.6170	0.1480	-0.58
O2	2.8598	0.2280	0.12
N	3.5012	0.1670	-0.58

Effect of the resistance geometry coefficient on the resistance of CNT-ISF.

It is assumed that the resistivity does not change during the stretching process, and the resistance change of the CNT-ISF fiber is entirely caused by resistance geometry coefficient (α). Therefore,

$$R_{total} = \gamma\frac{L}{S} = \gamma\alpha \tag{S1}$$

where γ, L, S represents resistivity, length, cross-sectional area of CNT-ISF fiber, respectively. $L = L_0 + \varepsilon L_0$, L_0 is the original length of CNT-ISF fiber.

$$R_{total} = R_i + \varepsilon R_i \tag{S2}$$

where $R_i = \gamma L_0/S$, represents the initial CNT-ISF fiber resistance at $\varepsilon = 0$. The comparison results(Fig. S4) show that the resistance change of the CNT-ISF fiber during the stretching process is not only caused by the change of the resistance geometry coefficient, but also the resistivity, that is, the internal structure.

The analysis of contact resistance between CNTs.

The macroscopic contact resistance between CNTs can be given as:[22-23]

$$R_{contact} = \frac{R_f}{WL_T} coth\left(\frac{L_c}{L_T}\right) \quad \text{(S3)}$$

where $L_T = \sqrt{R_f / R_{initial}}$ represents the distance over which most of the current transfers from one CNT to another CNT. $R_{initial}$ refers to the initial resistance of CNT-ISF ($R_{initial} = R_0 + R_{ion}$), R_f corresponds to the typical specific contact resistivities (the dimension is $\Omega \cdot m^2$), L_c and W refer to the contact length and width of CNTs, respectively. Moreover, L_c is related to the amount of CNTs' slippage (m)[24] during stretching. L_c and m can be described as:

$$L_c = L_0 - mL_0 \quad \text{(S4)}$$

$$m = \frac{\sigma}{2\rho_s \tau_s} \quad \text{(S5)}$$

Where σ is the stress of CNT-ISF fiber, ρ_s represents the aspect ratio of CNT-ISF fiber, *i.e.*, $\rho_s = L_0/2r_s$, L_0 and r_s represents the length and radius of the CNT-ISF fiber, τ_s refers to CNT-ISF fiber's shear stress and can be given as $\tau_s = \sigma_{my}/2$.

where σ_{my} represents the yield stress of ISF. Thus, Eq. (S5) can be written as:

$$m = \frac{\sigma}{2\rho_s \tau_s} = \frac{2r_s \ \sigma}{L_0 \ \sigma_{my}} \quad \text{(S6)}$$

The influence of CNT slippage on $R_{contact}$, therefore, can be obtained by substituting Eq. (S4) and (S6) into Eq. (S3):

$$R_{contact} = \frac{\sqrt{R_f}\sqrt{R_{initial}}}{2r_s} coth\left(\frac{L_0\sqrt{R_{initial}}}{\sqrt{R_f}} - \frac{2r_s\sqrt{R_{initial}}}{\sqrt{R_f}} \frac{\sigma}{\sigma_{my}}\right) \quad \text{(S7)}$$

Fabrication method of CNT fibers.

CNT fibers can also be prepared by floating catalyst chemical vapor deposition method as reported in literature.[25] The synthesis equipment includes liquid injection system, gas flow control system, liquid injection port, gas inlet, high temperature vertical tubular reactor, water tank and collection system. Firstly, the temperature of the vertical tubular reactor was raised to 1200-1300 ℃ at the rate of 1 ℃/min. At the same time, the water tank was filled with water to make the lower end of the furnace chamber in liquid seal state; argon was continuously injected at the flow rate of 100 mL/min for 12 hours to ensure that the air in the gas path is exhausted.

1-3 g of catalyst (ferrocene) and 1-3 g of promoter (thiophene) were dissolved in 94-98 g hydrocarbons or alcohols compound by ultrasound, and then the prepared reaction solution was continuously injected into reaction tube through a peristaltic pump at a certain rate through the injection port, and the carbon source was cracked under the hydrogen atmosphere of 1000-2000 mL/min flow rate. CNTs were self-assembled in reaction area by the decomposition of carbon atoms on the surface of the catalyst to obtain CNT aerogels and left the furnace cavity with airflow. The metal wire was extended from the bottom of the flume to the lower end of the reaction tube, and the aerogel was continuously pulled out and immersed in the water tank. The CNT film contracted into fiber and then collected by the spool wheel.

Molecular dynamics simulations.

The CNT-CNT model consists of a 3*3 single-walled carbon nanotube (CNT (6,6), 11.483×11.483×27.05 Å). In the CNT/ISF system, the SF and 20 Ca^{2+} was put around the CNT to strengthen the interface interaction between CNTs. SF molecule and covalent interaction between carbon atoms in CNT were described by OPLS-AA model[26] and Tersoff potential,[27] respectively. The Lennard-Jones parameters for non-bonded C-C interaction were $\epsilon = 0.105$ kcal/mol and $\mu = 3.851$ Å,[28] while that for SF is summarized in Tab. S3. Cross-interaction parameters between different species were determined using Lorentz−Berthelot combination rules. The electrostatic interactions and nonbonded interactions were calculated with the particle–particle-particle–mesh (PPPM) algorithm[29] and the 12-6 Lennard-Jones potential respectively, with both cutoff set to 1.2 nm.

All the MD simulations in this work were completed *via* the large-scale atomic/molecular massively parallel simulator (LAMMPS).[30] The periodic boundary conditions were imposed in three directions. A 100 Å slab of vacuum was inserted into the cell in the *x*-direction to separate each polymer from the next periodic imagine in the *z*-direction and eliminate artifacts from the periodicity of the simulation cell.[31,32] All systems were performed for 5 ns at 298 K, where the temperature is controlled *via* a Berendsen thermostat.[33] Both CNT-CNT and CNT-ISF system were equilibrated in the NPT ensemble, while the pressure along *y* and *z*-directions are setting as zero. The steered MD (SMD) simulation with the constant speed mode was used to pull the CNT in the *x*-direction and the motion of pulled single-walled CNT (SWCNT) in the other two directions was not constrained. The pulling speed and the spring constant were 1 m s^{-1} and 100 kcal (mol $Å^2$)$^{-1}$, respectively.

To capture the fracture mechanism of CNT-CNT and CNT-ISF composite, the CNT bundle and CNT-ISF were also simulated in the MD simulations. As shown in Fig. 6 nine CNT were inserted into the silk environment to form the CNT-ISF composite. The size of CNT-CNT and CNT-ISF

were 5.06×3.26×3.60 and 5.06×9.87×8.90 nm^3 along *x*-, *y*- and *z*-directions. The periodic boundary conditions were used in the three directions. The as-prepared systems were relaxed in the NPT ensemble, with a temperature of 300 K and a pressure of 1 bar for 500 ps. The timestep was 0.5 fs (determined by the force field of CNT, commonly used to investigate the mechanical property of CNT) and the Berendsen thermostat and barostat were adopted for temperature and pressure controls. After the system was fully relaxed, the composite films were stretched in the *x* direction with an engineering strain rate of 1×10^7 s^{-1} while the pressure along *y* and *z* direction was kept at ~1 bar. During the stretching process, the corresponding stress, strain, and atomic structure were recorded to obtain the mechanical and structural response of CNT-CNT and CNT-ISF composite. Through this simulation, how the existing of ISF affecting the fracture behavior of CNT, especially the fracture time of CNT can be predicted. However, such a model should be difficult to reproduce the entire modulus of the CNT-ISF composite because the CNT model was perfect without any defects, and the length can be seen as infinite, which was quite different from the experiment. defects or vacancies between CNTs might be introduced in future simulated work, to further explain the influence of defects between CNTs or the different packing style on the final material properties including strength and toughness modulus.

All density functional theory (DFT) calculations were performed with VASP (Vienna Ab-initio Simulation Package)[34] using plane-wave basis sets. An energy cutoff of 400 eV, the 1×1×1 Monkhorst-Pack mesh grid, and the generalized gradient approximation with PBE (Perdew-Burke-Ernzerhof) exchange-correlation functional[35] were used for all computations. All the structures were fully relaxed with the conjugate gradient method setting the convergence threshold on forces to 0.01 eV $Å^{-1}$. The binding energy is calculated as $E_{b1} = E_{Ca(II)/CNT} - E_{Ca(II)} - E_{CNT}$ for Ca^{2+}/CNT and $E_{b2} = E_{FA/CNT} - E_{FA} - E_{CNT}$ for FA/CNT, where $E_{Ca(II)}$, E_{CNT}, E_{FA} were the relaxed energy of Ca^{2+}, CNT and FA, respectively. $E_{Ca2+/CNT}$ and $E_{FA/CNT}$ were the total energy of the corresponding composite system.

References

1. W. Zhang, C. Ye, K. Zheng, J. Zhong, Y. Tang, Y. Fan, M. J. Buehler, S. Ling, D. L. Kaplan, Tensan silk-inspired hierarchical fibers for smart textile applications, *ACS Nano*, 2018, **12**, 6968-6977.
2. C. Ye, J. Ren, Y. Wang, W. Zhang, C. Qian, J. Han, C. Zhang, K. Jin, M. J. Buehler, D. L. Kaplan, S. Ling, Design and fabrication of silk templated electronic yarns and applications in multifunctional textiles, *Matter.*, 2019, **1**, 1411-1425.
3. G. Q. Fang, Z. K. Zheng, J. R. Yao, M. Chen, Y. Z. Tang, J. J. Zhong, Z. M. Qi, Z. Li, Z. Z. Shao, X. Chen, Tough protein-carbon nanotube hybrid fibers comparable to natural spider silks, *J. Mater. Chem. B*, 2015, **3**, 3940-3947.
4. Y. Wang, J. Guo, L. Zhou, C. Ye, F. G. Omenetto, D. L. Kaplan, S. Ling, Design, fabrication, and function of silk-based nanomaterials, *Adv. Funct. Mater.*, 2018, **28**.
5. E. Steven, W. R. Saleh, V. Lebedev, S. F. A. Acquah, V. Laukhin, R. G. Alamo, J. S. Brooks, Carbon nanotubes on a spider silk scaffold, *Nat. Commun.*, 2013, **4**, 8.
6. M. Z. Seyedin, J. M. Razal, P. C. Innis, G. G. Wallace, Strain-responsive polyurethane/PEDOT:PSS elastomeric composite fibers with high electrical conductivity, *Adv. Funct. Mater.*, 2014, **24**, 2957-2966.
7. R. Jalili, J. M. Razal, P. C. Innis, G. G. Wallace, One-step wet-spinning process of poly(3,4-ethylenedioxythiophene):poly(styrenesulfonate) fibers and the origin of higher

electrical conductivity, *Adv. Funct. Mater.*, 2011, **21**, 3363-3370.

8. R. Jalili, J. M. Razal, G. G. Wallace, Exploiting high quality PEDOT:PSS-SWNT composite formulations for wet-spinning multifunctional fibers, *J. Mater. Chem.*, 2012, **22**, 25174-25182.

9. R. Jalili, J. M. Razal, G. G. Wallace, Wet-spinning of PEDOT: PSS/functionalized-swnts composite: a facile route toward production of strong and highly conducting multifunctional fibers, *Sci. Rep-Uk.*, 2013, **3**, 7.

10. J. Foroughi, G. M. Spinks, G. G. Wallace, A reactive wet spinning approach to polypyrrole fibres, *J. Mater. Chem.*, 2011, **21**, 6421-6426.

11. Z. H. Tang, S. H. Jia, F. Wang, C. S. Bian, Y. Y. Chen, Y. L. Wang, B. Li, Highly stretchable core-sheath fibers via wet-spinning for wearable strain sensors, *ACS Appl. Mater. Interfaces*, 2018, **10**, 6624-6635.

12. A. J. Granero, J. M. Razal, G. G. Wallace, M. i. h. Panhuis, Elastic conducting carbon nanotube-laden SIBS fibers, International Conference On Nanoscience And Nanotechnology, Sydney, 2010, 80-83.

13. C. Xiang, W. Lu, Y. Zhu, Z. Sun, Z. Yan, C. C. Hwang, J. M. Tour, Carbon nanotube and graphene nanoribbon-coated conductive Kevlar fibers, *ACS Appl. Mater. Interfaces*, 2012, **4**, 131-136.

14. Z. Xu, C. Gao, Graphene chiral liquid crystals and macroscopic assembled fibres, *Nat. Commun.*, 2011, **2**, 571.

15. S. J. Ling, C. X. Li, J. Adamcik, S. H. Wang, Z. Z. Shao, X. Chen, R. Mezzenga, Directed growth of silk nanofibrils on graphene and their hybrid nanocomposites, *ACS Macro Lett.*, 2014, **3**, 146-152.

16. S. J. Ling, Q. Wang, D. Zhang, Y. Y. Zhang, X. Mu, D. L. Kaplan, M. J. Buehler, Integration of stiff graphene and tough silk for the design and fabrication of versatile electronic materials, *Adv. Funct. Mater.*, 2018, **28**, 10.

17. W. B. Zhong, C. Liu, C. X. Xiang, Y. X. Jin, M. F. Li, K. Liu, Q. Z. Liu, Y. D. Wang, G. Sun, D. Wang, Continuously producible ultrasensitive wearable strain sensor assembled with three-dimensional interpenetrating Ag nanowires/polyolefin elastomer nanofibrous composite yarn, *ACS Appl. Mater. Interfaces*, 2017, **9**, 42058-42066.

18. J. M. Gosline, P. A. Guerette, C. S. Ortlepp, K. N. Savage, The mechanical design of spider silks: From fibroin sequence to mechanical function, *J. Exp. Biol.*, 1999, **202**, 3295-3303.

19. E. Glenn, Resistivity of steel, https://hypertextbook.com/facts/2006/UmranUgur.shtml.

20. K. S. U. Schirmer, D. Esrafilzadeh, B. C. Thompson, A. F. Quigley, R. M. I. Kapsa, G. G. Wallace, Conductive composite fibres from reduced graphene oxide and polypyrrole nanoparticles, *J. Mater. Chem. B*, 2016, **4**, 1142-1149.

21. K. K. H. Yeung, K. P. Rao, Mechanical properties of boron and Kevlar-49 reinforced thermosetting composites and economic implications, *J. Eng. Sci.*, 2014, **10**, 19-29.

22. K. L. Grosse, M. H. Bae, F. Lian, E. Pop, W. P. King, Nanoscale joule heating, peltier cooling and current crowding at graphene-metal contacts, *Nat. Nanotechnol.*, 2011, **6**, 287-290.

23. G. K. Reeves, H. B. J. I. E. D. L. Harrison, Obtaining the specific contact resistance from transmission line model measurements, *IEEE Electron Device Lett.*, 1982, **3**, 111-113.

24. M. R. Piggott, *Load-bearing fibre composites*, Pergamon, 1980.

25. Q. Liu, M. Li, Y. Gu, S. Wang, Y. Zhang, Q. Li, L. Gao, Z. Zhang, Interlocked CNT networks with high damping and storage modulus, *Carbon*, 2015, **86**, 46-53.

26. W. L. Jorgensen, D. S. Maxwell, R. J. Tirado, Development and testing of the opls all-atom force field on conformational energetics and properties of organic liquids, *J. Am. Chem. Soc.*, 1996, **118**, 11225-11236.

27. L. Lindsay, D. A. Broido, Optimized tersoff and brenner empirical potential parameters for lattice dynamics and phonon thermal transport in carbon nanotubes and graphene, *Phys. Rev. B*, 2010, **82**, 205441.

28. Y. Wang, Z. Xu, Water intercalation for seamless, electrically insulating, and thermally transparent interfaces, *ACS Appl. Mater. Interfaces*, 2016, **8**, 1970-1976.

29. R. W. Hockney, J. W. Eastwood, *Computer simulation using particles*, Taylor and Francis, 1988.

30. S. Plimpton, *Fast parallel algorithms for short-range molecular dynamics*, SAND-91-1144, Other: ON: DE93018519, TRN: 93:002897 United States 10.2172/10176421 Other:

ON: DE93018519, TRN: 93:002897 OSTI, NTIS, GPO Dep, SNL English, Sandia National Labs., Albuquerque, NM (United States): 1993, p Medium: ED, Size: 40 p.

31. C. J. Fennell, J, D. Gezelter, Is the ewald summation still necessary? Pairwise alternatives to the accepted standard for long-range electrostatics, *J. Chem. Phys.*, 2006, **124**, 234104.

32. I.-C. Yeh, M. L.Berkowitz, Effects of the polarizability and water density constraint on the structure of water near charged surfaces: Molecular dynamics simulations, *J. Chem. Phys.*, 2000, **112**, 10491-10495.

33. H. J. C. Berendsen, J. P. M. Postma, W. F. Gunsteren, A. DiNola, J. R. Haak, Molecular dynamics with coupling to an external bath, *J. Chem. Phys.*, 1984, **81**, 3684-3690.

34. G. Kresse, J. Furthmüller, Efficient iterative schemes for ab initio total-energy calculations using a plane-wave basis set, *Phys. Rev. B*, 1996, **54**, 11169-11186.

35. J. P. Perdew, K. Burke, M. Ernzerhof, Generalized gradient approximation made simple, *Phys. Rev. Lett.*, 1996, **77**, 3865-3868.